

Supporting Information for

Ultrathin Two-Dimensional MnO₂/Graphene Hybrid Nanostructures for High Performance, Flexible Planar Supercapacitors

Lele Peng,^{†,‡} Xu Peng,^{||} Borui Liu,[‡] Changzheng Wu,^{,†} Yi Xie,^{*,†} Guihua Yu^{*,‡}*

[†]Hefei National Laboratory of Physical Sciences at the Microscale, University of Science and Technology of China, Hefei, Anhui, 230026, P. R. China;

[‡]Materials Science and Engineering Program and Department of Mechanical Engineering, The University of Texas at Austin, Austin, TX78712, USA;

^{||} School of Materials Science and Engineering, Wuhan Institute of Technology, Wuhan, Hubei, 430073, P. R. China.

Keywords: Planar Supercapacitor; Birnessite-MnO₂; Ultrathin nanosheets; All-solid-state; Layer-by-layer assembly; Energy storage

Table of contents

S1. Experimental details.....	2
S2. X-Ray Photoelectron Spectroscopy of δ -MnO ₂ bulk materials	3
S3. Structures of δ -MnO ₂ and the exfoliation process of layered δ -MnO ₂	3
S4. Tyndall Effect image of the as-exfoliated graphene, MnO ₂ nanosheets and the MnO ₂ /graphene hybrids.....	3
S5. TEM and AFM images of the as-exfoliated graphene and δ -MnO ₂ nanosheets.	4
S6. Demonstration of the hybrid thin films transferred onto smooth substrates, silicon wafer, quartz/glass, PET , respectively.....	5
S7 . The influence of electrode separation distances on capacitive behaviors.....	5
S8.Estimation of specific capacitance, energy density and power density.....	6
S9. The influence of weight percentage of MnO ₂ on specific capacitance.....	7
S10. Electrochemical properties of as-fabricated planar Supercapacitors.....	8
S11.Comparison of the traditional sandwiched type supercapacitors and planar supercapacitors	9
Table 1. Comparison of specific capacitances and energy density of the reported MnO ₂ /graphene and MnO ₂ /other carbon nanomaterials composite-based electrodes.....	10

S1. Experimental details

Synthesis of graphene, bulk δ -MnO₂ and δ -MnO₂ nanosheets: Graphene was obtained from the chemical reduction of graphene oxides. Graphene oxide was synthesized in a modified Hummer's method.¹ In brief, 9:1 mixture of concentrated H₂SO₄/H₃PO₄ (360:40 mL) was added to a mixture of graphite flakes (3.0 g) and KMnO₄ (18.0 g), producing a slight exotherm to 35~40 °C. The reaction was then heated to 50 °C and stirred for 12 h. The reaction was cooled to room temperature (RT) and poured onto ice (400 mL) with 30% H₂O₂ (3 mL). The dispersion was centrifuged under the speed of 2000 rpm for 30 mins, and the supernatant was decanted away. The remaining solid material was then washed in succession with 200 mL of water, 200 mL of 30% HCl, and 200 mL of ethanol; after each wash, the mixture was centrifuged under the speed of 2000 rpm for 30 mins. When the successive washing was done, the precipitate was dried at 60°C in a vacuum oven. Graphene was reduced using hydrazine in a reported method.² Hydrazine monohydrate (1 μ L for 3mg of GO, 98%, Aldrich) was subsequently added to the suspension. Additional stirring in an oil bath held at 80 °C for 12 h yielded a black precipitation of reduced graphene oxide powder. After cooling to RT, the powder was filtered through a fritted glass filter (medium pore size), followed by suction-drying under house-vacuum for 12 h. The resulting black material was dried under vacuum using a mechanical pump.

The bulk MnO₂ were synthesized in a reported method.³ Typically, 20 mL of a mixed aqueous solution of 0.6 M tetramethylammonium hydroxide (TMA·OH) and 3 wt % H₂O₂ was added to 10 mL of 0.3 M MnCl₂ ·4H₂O aqueous solution within 15s. The solution became dark brown immediately as the mixed aqueous solution added, showing the evidence that Mn²⁺ was oxidized to Mn⁴⁺. This whole mixed aqueous solution was vigorously stirred overnight in the ambient atmosphere at room temperature. After this mild oxidation process, the precipitate was washed with water and methanol and centrifuged at a very low speed of 2000 rpm for 20 mins, after which the precipitate was dried in a vacuum oven at 60 °C.

The layered structures could be exfoliated by solution and organic solvent. In our case, the layered H-type birnessite MnO₂ can be exfoliated by water solution. Experimentally, 10 mg bulk δ -MnO₂ was added into 20 mL water for ultrasonic treatment. After ultrasonic treatment for 10h, the dispersion was centrifuged under the speed of 1000 rpm, removing the un-exfoliated residues from the dispersions. As is well-known, the hydrazine reduced graphene is not easily exfoliated by water. Thus in our work, we adopted DMF to disperse graphene nanosheet. Similar to the process of exfoliating bulk δ -MnO₂, 1 mg graphene was dispersed in 20 mL DMF solvent. After ultrasonic treatment for 10h, the dispersion was centrifuged under the speed of 1000 rpm, removing the un-exfoliated graphites from the dispersions.

S2. X-Ray photoelectron spectroscopy of δ -MnO₂ bulk materials

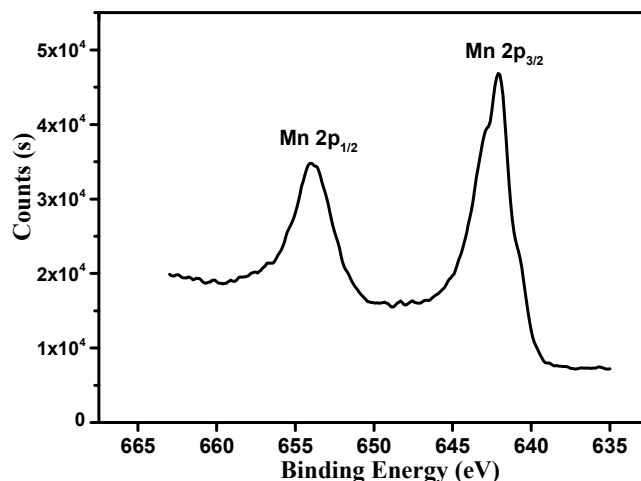


Figure S1. XPS of the bulk δ -MnO₂. A detailed chemical composition of as-prepared MnO₂ bulk material was probed by X-ray photoelectron spectroscopy (XPS) as shown above. According to the Mn 2p spectrum, two strong peaks centered at 642.1 and 654.1 eV corresponding to Mn⁴⁺ oxidation state were found, showing that Mn²⁺ was successfully oxidized to Mn⁴⁺. Specially, the curve of our sample matched with Mn(2p_{3/2}) spectrum of synthetic birnessite.⁵

S3. Structures of δ -MnO₂ bulk materials and the exfoliation process of layered δ -MnO₂

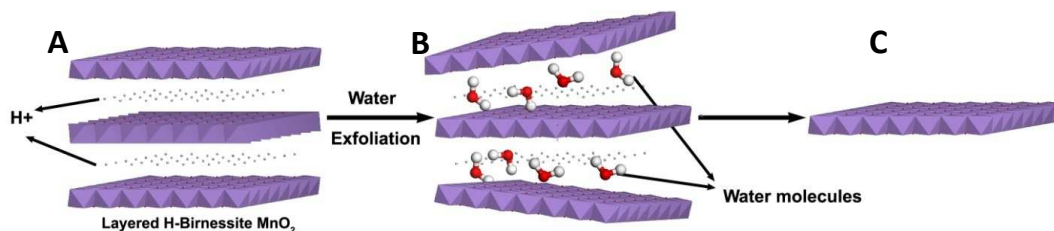


Figure S2. Exfoliation procedure of the MnO₂ ultrathin nanosheets. The layered bulk δ -MnO₂ structure is stabilized by the H⁺ intercalated between the MnO₂ layers (A). The weak van der Waals force can be broken by the ultrasonic force, thus the bulk δ -MnO₂ can be swelled by the water molecules. Experimentally, after an intercalation/extraction process of water molecules (B), the bulk δ -MnO₂ was exfoliated into single layered MnO₂ nanosheets (C), forming a homogeneous dispersion which exhibits a typical Tyndall effect.

S4. Tyndall effect image of the as-exfoliated graphene, MnO₂ nanosheets and the MnO₂/graphene hybrids

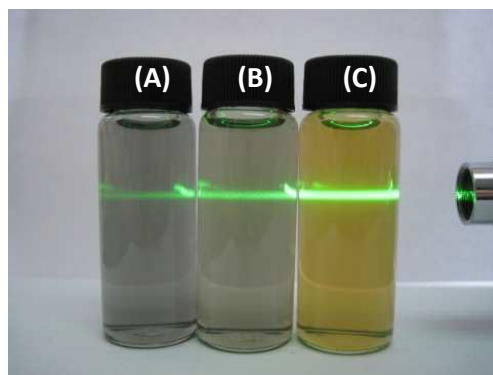


Figure S3. Optical image of the Tyndall Effect observed in as-obtained water dispersion for A. graphene (A), MnO_2 /graphene nanohybrids dispersion (B), ultrathin MnO_2 nanosheets dispersion (C). As shown above, the homogeneous laser light path displayed in the dispersion indicated that the layered MnO_2 was successfully exfoliated into nanosheets and these ultrathin nanosheets coexist with graphene, further forming homogeneous water dispersion. Note that the zeta potential result shows the $\delta\text{-MnO}_2$ nanosheet is electronegative. Given the fact that coagulation would occur when adding excessive graphene dispersion into MnO_2 nanosheet dispersion, the graphene dispersion is electropositive in this sense. It is possibly because hydrazine reduced graphene will leave NH_4^+ absorbed on graphene surfaces, resulting in the electropositivity of graphene.

S5. TEM and AFM images of as-exfoliated graphene and $\delta\text{-MnO}_2$ nanosheets

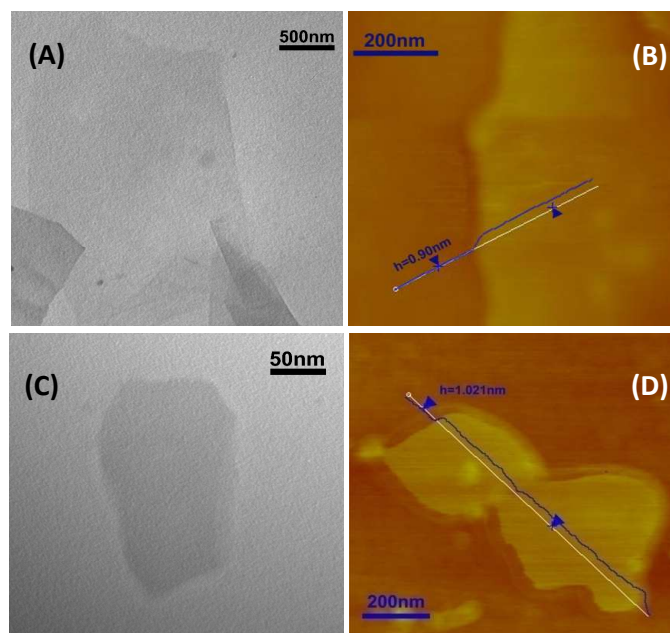


Figure S4. TEM and AFM images of graphene and $\delta\text{-MnO}_2$ nanosheets. (a) TEM image of graphene showing the size of $\sim 4 \mu\text{m}$. (b) Tapping mode AFM image of graphene nanosheet, indicating the thin thickness of $\sim 0.9 \text{ nm}$. (c) TEM image of $\delta\text{-MnO}_2$ nanosheet. (d) Tapping mode AFM image of a $\delta\text{-MnO}_2$ nanosheet, indicating the thin thickness of $\sim 1.0 \text{ nm}$.

S6. Demo of hybrid thin films transferred onto various substrates: silicon wafer, quartz/glass, PET.

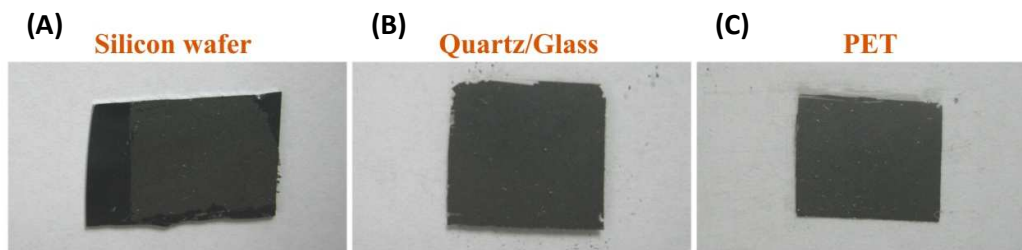


Figure S5. Optical images of the transferred hybrid thin film on Silicon wafer (A), Quartz (B) and PET substrates(C).

S7. The influence of electrode separation distances on capacitive behaviors

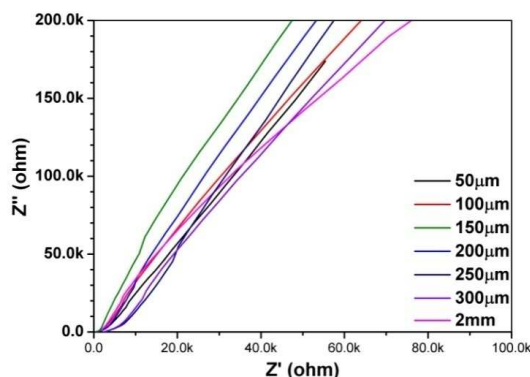


Figure S6: Comparison of impedance curves for supercapacitors with different separation distances. The supercapacitor with $\sim 150 \mu\text{m}$ separation possesses the best capacitive behavior among all control experiments with the separation distances from 50, 100, 150, 200, 250, 300 μm and 2 mm.

To explore the influence of electrode separation on the capacitor behaviors, we fabricated the planar supercapacitors with electrode separations (distance between MnO_2/G strips) from 50 μm to 2 mm. To evaluate the capacitive behavior of the planar supercapacitor, we performed Electrochemical Impedance Spectroscopy (EIS) tests using a two-electrode configuration. To our knowledge, the straight line at the low frequency shown in the Nyquist plots nearly parallel to the imaginary axis indicated the ideal capacitive behavior of the device. As is shown in **Figure S6**, the slope of the straight line at the low frequency acquired from the device with a 150 μm electrode separation is relatively larger than that of other devices, indicating the best capacitive behavior of the device. Therefore, we fabricated planar supercapacitors with the electrode separation of $\sim 150 \mu\text{m}$.

In the present work, the main objective is to illustrate different electrochemical performances of planar supercapacitors based on the utilization of two-dimensional ultrathin- $\text{MnO}_2/\text{graphene}$ nanohybrid. Thus we systematically compared different planar

supercapacitors at the same electrode separation distance (150 μm in this study). Since the electrolyte ions are transported two-dimensionally in our designed devices, planar supercapacitors with the same electrode separation have a same ion migration distance, so that we could eliminate the systematic errors from the electrode separation for evaluating the electrochemical performance of planar supercapacitors.

S8. Estimation of specific capacitance, energy density and power density

The electrochemical performance of supercapacitor based on the planar hybrid thin film was studied by galvanostatic charge/discharge measurements. As shown in Figure 4(C) (D), the galvanostatic charge/discharge curves of the planar supercapacitors were conducted using a two-electrode system to calculate the specific capacitance under different current density (from 0.5 A/g to 10 A/g). From the CD chart, the specific capacitance can be derived based on the following equation:

$$C = I \frac{\Delta t}{m \Delta V} \quad (1)$$

in which I is the constant current applied to the planar supercapacitor; Δt and ΔV represent the discharging time and discharging voltage range respectively; and m is the mass loading of the electrodes. On the basis of the galvanostatic charge-discharge results, the specific capacitances of planar supercapacitor were determined.

Energy density (E) and power density (P) were obtained from the CV curves and CD curves in Figure 4, derived based on the following equations:

$$E = \frac{1}{2} C V^2 \quad (2)$$

$$P = \frac{E}{\Delta t} \quad (3)$$

where C is the specific capacitance of the device, V is the working voltage, and Δt represents the discharging time. As is shown in the Ragone plots, the $\delta\text{-MnO}_2/\text{graphene}$ hybrid based planar supercapacitors deliver a high energy density of 17 Wh/kg at a high power density of 2520 W/kg, much superior to graphene based planar supercapacitor. Moreover, the maximum energy density of 18.64 Wh/kg and the highest power density of 12.6 kW/kg are achieved using our hybrid based planar supercapacitor at an operation voltage of 0.7 V.

S9. The influence of weight percentage of MnO_2 on specific capacitance

We adopted the pseudocapacitive $\delta\text{-MnO}_2$ nanosheets with high redox capacitance (theoretically ~ 1300 F/g for MnO_2) to enhance the specific capacitance of the planar supercapacitor. In order to explore the influence of the weight percentage of MnO_2 on the specific capacitance, we conducted two control experiments at the weight percentage of $\sim 25\%$, $\sim 75\%$, and the results are shown in **Figure S7**. Compared with $\sim 66\%$ MnO_2 in the maintext, the specific capacitances acquired from supercapacitors with 25% and 75% weight percentage of MnO_2 display inferior capacitance performance. In the control experiments, excessive

loading of MnO_2 on graphene successively increased the electrical resistance of the electrodes, rendering less effective electron transport and resulting in poor specific capacitance. Furthermore, as excess MnO_2 nanosheets were added, severe aggregation would form, leading to the inferior mechanical properties and flexibilities of the as-obtained planar supercapacitors. In contrast, when less pseudocapacitive MnO_2 nanosheets were integrated on graphene, the effective utilization of hybrid graphene/ MnO_2 nanosheets cannot achieve the maximum, rendering a lower specific capacitance of the supercapacitor.

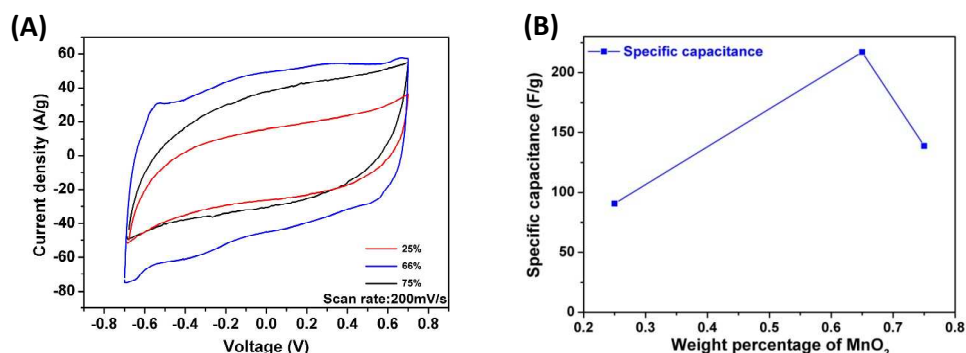


Figure S7: Electrochemical performance of the planar supercapacitor with different weight percentage of MnO_2 (25%, 66% and 75%). (a) CV curves acquired from the planar supercapacitors with different weight percentages of MnO_2 at the scan rate of 200 mV/s. (b) Comparison of specific capacitance values for the supercapacitors with different weight percentages of MnO_2 .

S10. Electrochemical properties of as-fabricated planar supercapacitors

The electrochemical performance of the $\text{MnO}_2/\text{Graphene}$ hybrids planar supercapacitor and the control group was evaluated using a two-electrode method by CHI660D battery testing system.

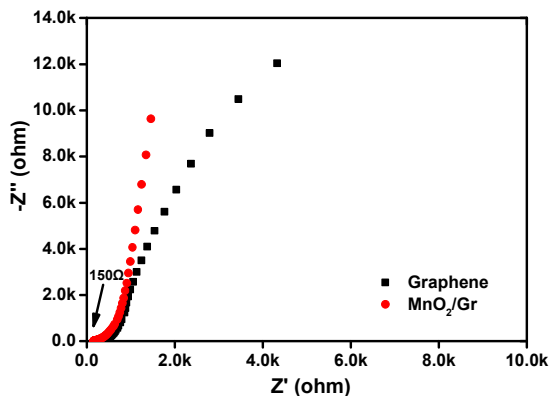


Figure S8. Comparison of impedance curves for planar supercapacitors based on $\delta\text{-MnO}_2/\text{Graphene}$ hybrid film and based on graphene-only. As the Nyquist plots shown in Figure S6, the straight line at the low frequency nearly parallel to the imaginary axis indicated the ideal capacitive behavior of the device. Notably, the capacitive behavior of the planar supercapacitor based on 2D $\delta\text{-MnO}_2/\text{graphene}$ hybrid thin film has been enhanced by integrating $\delta\text{-MnO}_2$ nanosheet on graphene, since the slope of the straight line at the low frequency is much bigger than that of the planar supercapacitor based on graphene.

Electrolyte: Electrolyte is an essential element for planar supercapacitors. In our initial work, we adopted PVA (polyvinyl alcohol) electrolyte to avoid chemical reactions at electrode and to achieve all-solid-state condition. It has been a challenge for developing neutral gel electrolyte because common metal salts such as Na_2SO_4 and KCl , would be easily crystallized out during the gel preparation. Moreover, we find out the $\text{PVA}/\text{H}_3\text{PO}_4$ electrolyte have an advantage over $\text{PVA}/\text{H}_2\text{SO}_4$ in cycling stability. The excellent cyclability is due in large part to the fact that the acidity of H_3PO_4 is weaker than H_2SO_4 , so it can reduce the corrosion of the electrodes.

In this work, the $\text{PVA}/\text{H}_3\text{PO}_4$ gel electrolyte was chosen to stabilize the $\text{MnO}_2/\text{Graphene}$ nanohybrids electrode, successfully maintaining the framework of MnO_2 nanosheets. The remarkable cycling performance of the planar supercapacitors exhibits a capacitance retention rate more than 92% after 7000 cycles as well as no notable capacitance loss after more than three month delay.

S11. Comparison of the traditional sandwiched type supercapacitors and planar supercapacitors

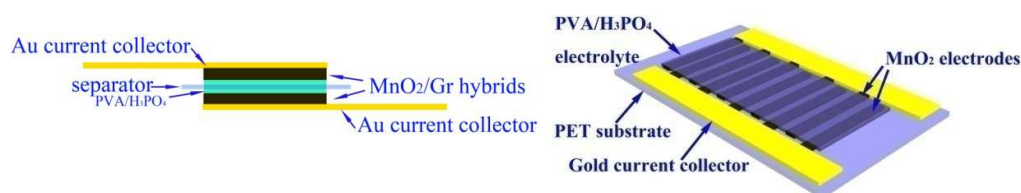


Figure S9. Schematic comparison of the traditional sandwich-type supercapacitor (left) and planar supercapacitor (right).

Two separate PET substrates were utilized to create the initial large scale planar hybrid based electrodes by a transfer method (Same as the one used for planar supercapacitor in our work). After cropping the film to the desired size, the polymer-gel electrolyte was applied onto both the electrodes, and then two separate electrodes with the dried electrolytes were sandwiched together separated by a separator. The devices were then tested for their electrochemical performance. In the traditional sandwich-type supercapacitor, the electrolyte ions were absorbed at the surfaces of the electrodes. Triggered by the applied voltage, the ions penetrated into the electrodes. While the cations and anions in the electrolyte should pass through the separator, which will hinder the fast charging/discharging process. On the contrary, the electrolyte ions are transported in 2D fashion in the planar configuration, shortening the ion travel distance by eliminating the necessity of a separator which is indispensable in the sandwich-type ECs to prevent electrical short. The δ -MnO₂ ultrathin nanosheets integrated on graphene decrease highly densely stacking of graphene sheets and smooth the planar path way of the ions, thus this open structure allows for more electrolyte ions to penetrate efficiently into the hybridized film for enhancing the utilization of active surface areas. Additionally, the hybridized δ -MnO₂/graphene interlayer areas introduce extra interfaces, in which the conducting graphene would facilitate the electron conduction through as-formed δ -MnO₂/graphene interfaces during charging/discharging process. In effect, the hybrid films produced the in-plane ion migration channel, promoting the electrolyte ions to transport two-dimensionally but not to travel through the overlapped edges, which will significantly shorten the ion diffusion distance and enhance the diffusion co-efficiency.

Table 1. Comparison of specific capacitances and energy density of the reported MnO₂/graphene and MnO₂/other carbon nanomaterials composite-based electrodes

Material Samples	Cs (F/g)	Energy density(Wh/kg)	Ref#
Traditional MnO₂/graphene composites			
MnO ₂ nanoparticles/graphene	365(5 mV s ⁻¹)	12.6	6
MnO ₂ nanowires/graphene (Asymmetric)	31(0.5 A g ⁻¹)	30.4	7
Flowerlike MnO ₂ /graphene	328(0.5mA cm ⁻²)	11.4	8
MnO ₂ nanostructured textiles/graphene	315(2 mV s ⁻¹)	12.5	9
MnO ₂ /graphene nanosheet	235(20 mV s ⁻¹)	33.1	10
MnO ₂ nanowires/graphene oxide	216(0.15 A g ⁻¹)	/	11
MnO ₂ nanosheets/Reduced graphene oxide	188 (0.25 A g ⁻¹)	/	12
Traditional MnO₂/carbon nanomaterials composites			
MnO ₂ nanowires/carbon nanotube paper	168(77 mA g ⁻¹)	/	13
MnO ₂ thin film/carbon nanofibers	313(50 mV s ⁻¹)	32	14
MnO ₂ /mesoporous carbon	218(0.1 A g ⁻¹)	/	15
Nanoflower MnO ₂ /CNT array	199(0.5 A g ⁻¹)	/	16
MnO ₂ / Nanostructured graphene	246F/cm ³ (10 mV s ⁻¹)	/	17
In-plane supercapacitor			
Pristine Graphene(control group)	138	8.03	
VS ₂ nanosheet	317 F/cm ³	/	18
Present work	267(0.2 A/g)	18.64	

References

- (1) Marcano, D. C.; Kosynkin, D. V.; Berlin, J. M.; Sinitskii, A.; Sun, Z.; Slesarev, A.; Alemany, L. B.; Lu, W.; Tour, J. M. *ACS Nano* **2010**, *4*, 4806-4814.
- (2) Park, S.; An, J.; Potts, J. R.; Velamakanni, A.; Murali, S.; Ruoff, R. S. *Carbon* **2011**, *49*, 3019-3023.
- (3) Omomo, Y.; Sasaki, T.; Wang, L.; Watanabe, M. *J. Am. Chem. Soc.* **2003**, *125*, 3568-3575.
- (4) Devaraj, S.; Munichandraiah, N. *J. Phys. Chem. C* **2008**, *112*, 4406-4417.
- (5) Nesbitt, H. W.; Banerjee, D. *American Mineralogist*. **1998**, *83*, 305-315.
- (6) Chen, C.; Fan, C.; Lee, M.; Chang, J. *J. Mater. Chem.* **2012**, *22*, 7697-7700.
- (7) Wu, Z.; Ren, W.; Wang, D.; Li, F.; Liu, B.; Cheng, H. *ACS Nano* **2010**, *4*, 5835-5842.
- (8) Cheng, Q.; Tang, J.; Ma, J.; Zhang, H.; Shinya, N.; Qin, L. *Carbon* **2011**, *49*,

2917–2925.

- (9) Yu , G.; Hu , L.; Vosgueritchian , M.; Wang , H.; Xie , X.; McDonough, J. R.; Cui, X.; Cui, Y.; Bao, Z. *Nano Lett.* **2011**, *11*, 2905–2911.
- (10) Rakhi, R. B.; Chen, W.; Cha, D.; Alshareef, H. N. *J. Mater. Chem.* **2011**, *21*, 16197–16204.
- (11) Chen, S.; Zhu, J.; Wu, X.; Han, Q.; Wang, X. *ACS Nano* **2010**, *4*, 2822–2830.
- (12) Zhang, J.; Jiang, J.; Zhao, X. *J. Phys. Chem. C* **2011**, *115*, 6448–6454.
- (13) Chou, S.; Wang, J.; Chew, S.; Liu, H.; Dou, S. *Electrochem. Commun.* **2008**, *10*, 1724–1727.
- (14) Liu, J.; Esnner, J.; Li, J. *Chem. Mater.* **2010**, *22*, 5022–5030.
- (15) Peng, Y.; Chen, Z.; Wen, J.; et al. *Nano Res.* **2011**, *4*, 216–225.
- (16) Zhang, H.; Cao, G.; Wang, Z.; et al. *Nano Lett.* **2008**, *8*, 2664–2668.
- (17) Lee, S.; Kim, J.; Chen, S.; Hammond, P.; Shao-Horn, Y. *ACS Nano* **2010**, *4*, 3889–3896.
- (18) Feng, J.; Sun, X.; Wu, C.; Peng, L.; Lin, C.; Hu, S.; Yang, J.; Xie, Y. *J. Am. Chem. Soc.* **2011**, *133*, 17832–17838.